

# Light-valley interactions in 2D semiconductors

Kin Fai Mak<sup>1,2\*</sup>, Di Xiao<sup>3\*</sup> and Jie Shan<sup>1,2\*</sup>

**The emergence of two-dimensional Dirac materials, particularly transition metal dichalcogenides (TMDs), has reinvigorated interest in valleytronics, which utilizes the electronic valley degree of freedom for information storage and processing. Here, we review the basic valley-dependent properties and their experimental demonstrations in single-layer semiconductor TMDs with an emphasis on the effects of band topology and light-valley interactions. We also provide a brief summary of the recent advances on controlling the valley degree of freedom in TMDs with light and other means for potential applications.**

The quantum degrees of freedom of electrons play important roles in many areas of modern science and technology. In particular, they form the basis for information storage and processing. The ability to understand and manipulate a new quantum degree of freedom can potentially open up a new paradigm for information technology. Electrons in certain crystalline solids possess a valley degree of freedom in addition to charge and spin. The valley degree of freedom describes which of the multiple degenerate energy extrema (or valleys) in the conduction or valence bands the electrons occupy. Because the valleys are often separated by a large crystal momentum, the electron intervalley scattering time can be long in clean materials with few atomic-scale defects. As a result, the electronic valley has been proposed as an information carrier for a new technology known as valleytronics. Table 1 briefly compares valley with charge and spin, two well-known quantum degrees of freedom of electrons, as information carriers.

Many crystalline solids are known to host electronic valleys. They include conventional semiconductors or insulators such as Si (ref. <sup>1</sup>), diamond<sup>2</sup> and AlAs (ref. <sup>3</sup>), semimetal Bi (ref. <sup>4</sup>), two-dimensional (2D) materials such as graphene<sup>5,6</sup> and TMDs<sup>7,8</sup>, and Weyl semimetals<sup>9,10</sup>. The idea of valleytronics has been explored for some time, but in most materials it is difficult to address and control the valley state of electrons due to the lack of valley-dependent physical quantities. The emergence of 2D materials with hexagonal lattices, particularly TMDs, has reinvigorated the field in the past several years. These materials have two valleys at the K and K' (or -K) points in the Brillouin zone, which are time-reversal copies of each other<sup>5</sup>. As we discuss below, the valley-contrasting Berry curvature  $\Omega$  and orbital magnetic moment  $\mu_v$  that interact directly with applied electric and magnetic fields, respectively, have provided powerful handles to control the valley degree of freedom. However, not all 2D materials with hexagonal lattices possess non-vanishing Berry curvatures and orbital magnetic moments. Being pseudovectors,  $\Omega(\mathbf{k})$  and  $\mu_v(\mathbf{k})$  are odd under time reversal ( $\Omega(\mathbf{k}) = -\Omega(-\mathbf{k})$ , where  $\mathbf{k}$  is the crystal momentum) and even under inversion ( $\Omega(\mathbf{k}) = \Omega(-\mathbf{k})$ ). Therefore, valley-contrasting phenomena can manifest only in materials with broken inversion symmetry<sup>5</sup>. (This symmetry argument does not consider spins, which also need to be flipped under time reversal.) These materials include single-layer hexagonal TMDs and gapped graphene.

This Review will focus on the understanding and manipulation of the electronic valleys in single-layer hexagonal TMDs (MX<sub>2</sub>) that are semiconductors. They consist of a layer of transition metal atoms

(M = Mo, W) between two layers of chalcogen atoms (X = S, Se, Te) in a trigonal prismatic structure<sup>11</sup> (Fig. 1a). The lattice possesses three-fold rotational symmetry, out-of-plane mirror symmetry, and, most importantly, broken inversion symmetry. These materials are direct-gap semiconductors with gaps located at the K and K' points<sup>12,13</sup> (Fig. 1b). Since the optical gaps are in the infrared-visible spectral range and the light-matter interactions are extremely strong<sup>11</sup>, optical control and probe are particularly effective and suitable for these materials. Furthermore, high-mobility electron transport has been recently reported in these materials<sup>14,15</sup>, making them truly unique for valleytronics.

We will start with a discussion of the two valley-contrasting physical quantities, namely the Berry curvature and the orbital magnetic moment, and their influence on the basic electrical transport and optical properties of single-layer TMDs. This will be followed by a brief review of the recent experimental advances on controlling the valley degree of freedom in TMDs optically and electrically. We will conclude with a brief outlook on future challenges and opportunities in TMD-based valleytronics. We refer the reader to other recent reviews for more detailed discussions on the physics of spin and pseudospins<sup>16</sup>, electronics<sup>17</sup>, photonics and optoelectronics<sup>11,18</sup> of 2D TMDs.

## Berry curvature and valley Hall effect

We first give a brief overview of the Berry phase- and Berry curvature-related properties of Bloch bands in 2D Dirac materials, which underlie many valley-contrasting physical phenomena<sup>5-7</sup>. The simplest Hamiltonian that describes a 2D Dirac system is<sup>5-7,16</sup>

$$H_{\text{Dirac}} = \tau k_x \sigma_x + k_y \sigma_y + \Delta \sigma_z \quad (1)$$

where  $\tau = \pm 1$  is the valley index (+1 for K and -1 for K'),  $\mathbf{k} = (k_x, k_y)$  is the crystal momentum counted from the K or K' point,  $2\Delta$  is the bandgap ( $\Delta = 0$  for graphene and  $\Delta \neq 0$  for single-layer TMDs), and  $\sigma$  is the Pauli matrices defined in the space of atomic orbitals that make up the Bloch functions at the band edge ( $\mathbf{k} = 0$ ). The band dispersion of  $H_{\text{Dirac}}$  near the K and K' points is shown in Fig. 1b for  $\Delta \neq 0$ . Because this Review mainly concerns the valley-dependent physics, spin-orbit coupling<sup>7</sup> is neglected here for simplicity. It is useful to consider  $H_{\text{Dirac}}$  as the Hamiltonian for a fictitious spin coupled to a magnetic field  $\tilde{\mathbf{B}}\hat{\mathbf{n}} = (\tau k_x, k_y, \Delta)$ , where  $\hat{\mathbf{n}}$  is the unit vector along the magnetic field (Fig. 1c). When an electron moves along a circle in momentum space around  $\mathbf{k} = 0$ ,  $\hat{\mathbf{n}}$  traces out a circle on a

<sup>1</sup>Department of Physics and School of Applied and Engineering Physics, Cornell University, Ithaca, NY, USA. <sup>2</sup>Kavli Institute at Cornell for Nanoscale Science, Ithaca, NY, USA. <sup>3</sup>Department of Physics, Carnegie Mellon University, Pittsburgh, PA, USA. \*e-mail: [kinfai.mak@cornell.edu](mailto:kinfai.mak@cornell.edu); [dixiao@cmu.edu](mailto:dixiao@cmu.edu); [jie.shan@cornell.edu](mailto:jie.shan@cornell.edu)

**Table 1 | Comparison of charge, spin and valley as information carriers**

	Charge	Spin	Valley
Physical origin	Electron charge	Electron spin angular momentum	Electron sublattice orbital angular momentum
Pros	Direct response to an electric field Easy to initiate, control and detect Direct optoelectronic coupling to light intensity High speed	Non-volatile No direct Joule heating Long spin lifetime and decoherence time Direct coupling to photon spins	Large Berry curvature hotspot for physical access with electric and magnetic fields No direct Joule heating Long valley lifetime (especially with spin-valley locking) Direct coupling to photon spins Non-volatile (in a magnetic heterostructure)
Cons	Joule heating Typically volatile Fast decoherence due to electron scattering	No direct response to an electric field Initiation, control and detection typically rely on indirect spin-charge conversion Low spin-charge conversion efficiency May require magnetic field	No direct response to an electric field Initiation, control and detection typically rely on indirect valley-charge conversion Low valley-charge conversion efficiency May require magnetic field Fast valley decoherence (so far)

unit sphere. As a result, the two-component spinor wavefunction picks up a quantal phase (the Berry phase), which is equal to half of the solid angle traced out by  $\hat{\mathbf{n}}$ . Moreover, because of the opposite sign of  $\tau$ , the Berry phase is of opposite sign at the two valleys, making it possible to distinguish them using the Berry phase. However, if the bandgap  $\Delta = 0$ , the circle traced out by  $\hat{\mathbf{n}}$  would be the equator of the unit sphere. In this case, the Berry phase at the two valleys would be  $\pi$  and  $-\pi$  (ref. <sup>19</sup>), which are indistinguishable since a phase is defined modulo  $2\pi$ . Only when a gap is opened by inversion symmetry breaking, does the Berry phase at the two valleys become distinguishable<sup>5,6</sup>. This is the underlying reason why the electronic valleys of single-layer TMDs can be readily addressed and controlled whereas in graphene it is difficult.

**Berry curvatures.** The Berry phase can also be considered as a magnetic flux in momentum space<sup>19</sup>. The corresponding magnetic field is the Berry curvature  $\Omega$ . Analogous to a real magnetic field, which is the curl of the vector potential in position space, the Berry curvature is the curl in momentum space ( $\nabla_{\mathbf{k}} \times$ ) of the Berry vector potential  $\mathbf{A}(\mathbf{k}) = i\langle u | \nabla_{\mathbf{k}} | u \rangle$  (ref. <sup>19</sup>), where  $u$  is the periodic part of the Bloch function. Because of the broken inversion symmetry in single-layer TMDs,  $\Omega(\mathbf{k})$  is finite at the K and K' points and has opposite sign for the conduction and the valence bands (Fig. 1d). The Berry phase<sup>19</sup> can be obtained by an areal integral of  $\Omega(\mathbf{k})$  in momentum space.

**The valley Hall effect.** The presence of Berry curvature (magnetic field in momentum space) can significantly modify the electron dynamics and generate new electrical transport phenomena. In particular, in the presence of an applied electric field  $\mathbf{E}$ , the electrons gain an anomalous velocity<sup>19</sup>

$$\mathbf{v}_a = \frac{e}{\hbar} \mathbf{E} \times \Omega \quad (2)$$

where  $e$  and  $\hbar$  denote the elementary charge and the Planck constant, respectively. This is analogous to the consequence of a Lorentz force for electrons moving under a perpendicular magnetic field. Since the Berry curvature is opposite at the two valleys (Fig. 1d), the anomalous velocity leads to the valley Hall effect (VHE)<sup>5–7,19</sup>, that is, carriers from the two valleys flow in opposite transverse directions in response to the bias electric field  $\mathbf{E}$  (in absence of any applied magnetic field). This opens the possibility of controlling the electronic valleys by an electric field. Furthermore, as we discuss below, because the K and K' electrons carry an orbital

magnetic moment  $\mu_v$  of opposite sign<sup>5–7,19,20</sup>, their transverse flow driven by the VHE generates a pure angular momentum current  $\mathbf{J}_v$  (valley current) without a net charge current (Fig. 2a). Such a transverse valley current leads to an accumulation of excessive K (K') electrons on the left (right) edges of the sample, and a finite valley polarization (that is, population imbalance) of opposite sign arises within the valley mean free path from the edges<sup>5</sup>.

The VHE in single-layer TMDs was first demonstrated by detecting a Hall voltage while circularly polarized light was employed to create an imbalance between the two valleys in a MoS<sub>2</sub> Hall bar device<sup>21</sup>. Subsequently, the effect was directly imaged in MoS<sub>2</sub> transistors by magneto-optical Kerr rotation microscopy<sup>22,23</sup> (Fig. 2a,b). The experimental scheme is similar to that used to detect the spin Hall effect<sup>24</sup>. The edge valley polarization was imaged through the polarization rotation or ellipticity of linearly polarized probe light near the fundamental exciton resonance. These experiments rely on the exclusive coupling between the valley degree of freedom and handedness of circularly polarized light discussed in the next section. These studies are further contrasted with the study of the VHE in bilayer 2H-MoS<sub>2</sub> (refs <sup>21,22</sup>) (Fig. 2c). Pristine 2H-bilayers are inversion symmetric (in contrast, 3R-MoS<sub>2</sub> is non-centrosymmetric for any layer thicknesses). The Berry curvature in bilayer 2H-MoS<sub>2</sub> is zero and the VHE is absent. The inversion symmetry can be broken by application of a vertical electric field through gating<sup>25</sup>. The Berry curvature and the VHE can thus be continuously tuned by the vertical electric field<sup>25</sup>. In particular, the direction of the valley current can be switched by reversing the direction of the vertical electric field<sup>22</sup> (Fig. 2c,d).

### Valley magnetic moment and optical selection rules

The broken inversion symmetry also allows the existence of an orbital magnetic moment  $\mu_v$ . Intuitively, it can be regarded as arising from the self-rotation of the electron wavepacket<sup>5</sup>. Since the motion is in the 2D plane, the orbital magnetic moment is out of plane. For a system described by the 2D Dirac Hamiltonian of equation (1), the orbital magnetic moment has a simple expression at the K and K' points  $\mu_v = \tau \frac{e\hbar}{2m^*} \hat{\mathbf{z}}$  (ref. <sup>5</sup>), where  $m^*$  ( $>0$ ) is the effective mass of the Bloch band and  $\hat{\mathbf{z}}$  is the out-of-plane unit vector. In contrast to the Berry curvature, the orbital magnetic moment carries identical sign for the conduction and the valence bands at the same valley. It behaves like a spin magnetic moment with an effective Bohr magneton  $\pm \frac{e\hbar}{2m^*}$  with the upper and lower sign for the conduction and valence band, respectively. As a result, the conduction and the valence states at the K point carry a valley orbital angular

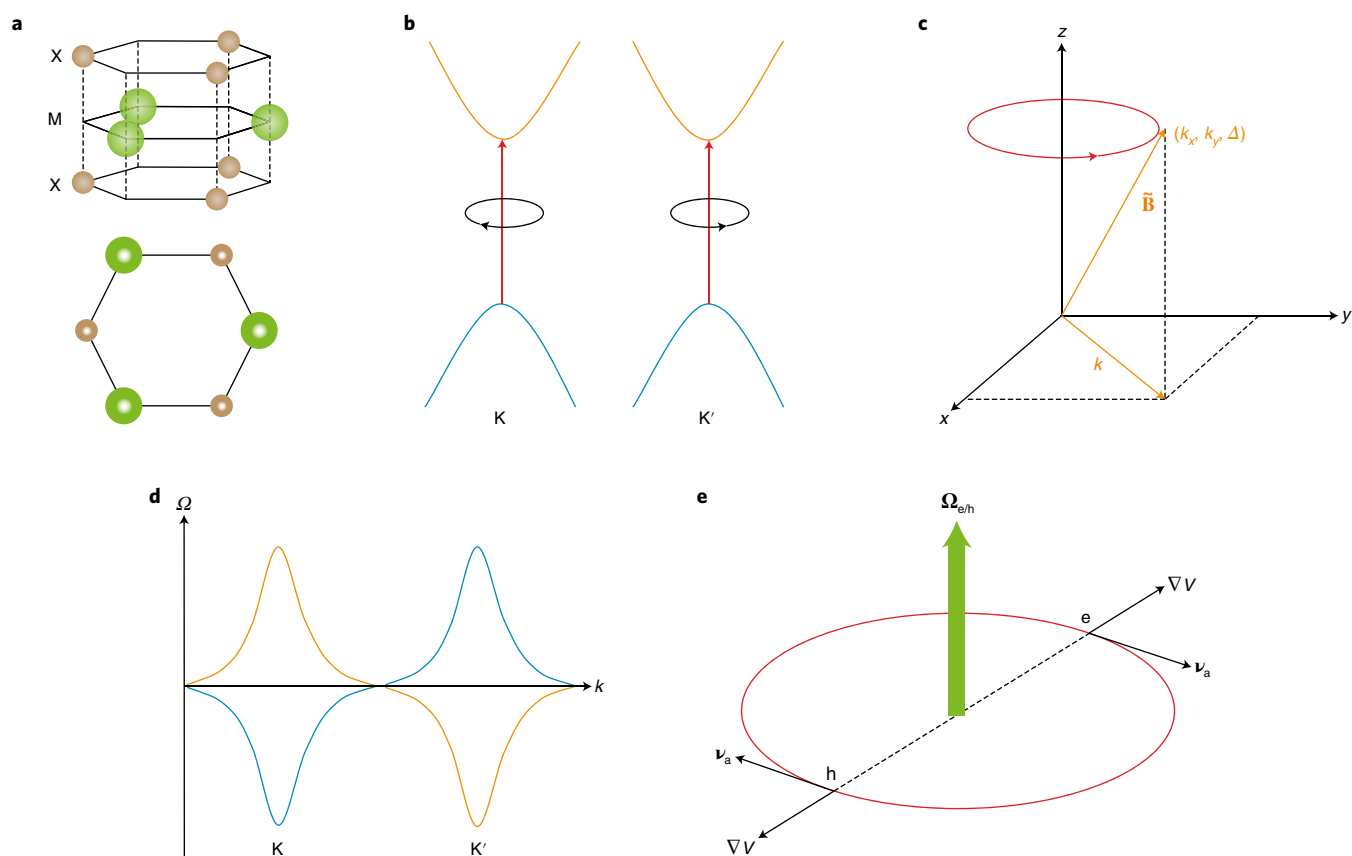


**Fig. 1 | Dirac electrons in single-layer TMDs.** **a**, Side and top view of the crystal structure of hexagonal TMDs ( $\text{MX}_2$ ,  $\text{M} = \text{Mo}, \text{W}$ ;  $\text{X} = \text{S}, \text{Se}, \text{Te}$ ). **b**, Electronic band dispersions near the  $\text{K}$  and  $\text{K}'$  points of the Brillouin zone. The interband transitions in the two valleys (red arrows) are allowed for circularly polarized light of opposite helicity. **c**, Fictitious magnetic field  $\tilde{\mathbf{B}}$ , as defined in the text, couples to the valley pseudospin. A Berry phase is acquired when an electron undergoes an adiabatic rotation along the red circle. **d**, Berry curvature distribution for the conduction (orange) and valence band (blue) near the  $\text{K}$  and  $\text{K}'$  points. **e**, The electron (e) and hole (h) in each valley form an exciton under a central potential  $V$ . They experience an anomalous velocity  $\mathbf{v}_a$  due to the Berry curvatures ( $\Omega_{e/h}$ ), lifting the degeneracy between the left- and right-rotating exciton states.

momentum  $\hbar/2$  and  $-\hbar/2$ , respectively. The sign is switched at the  $\text{K}'$  valley to satisfy the time-reversal symmetry. The orbital magnetic moment couples to an applied magnetic field  $\mathbf{B}$  via a Zeeman-like interaction,  $-\boldsymbol{\mu}_v \cdot \mathbf{B}$ . Below we discuss in more detail how the valley magnetic moment allows the control of the valley degree of freedom in single-layer TMDs by circularly polarized light and an out-of-plane magnetic field.

**Optical selection rules.** Let us consider the total magnetic quantum number of the electronic states near the  $\text{K}$  and  $\text{K}'$  points. The wavefunction for the conduction band is largely composed of the transition metal atom  $d_{z^2}$  orbital with a magnetic quantum number 0, and for the valence band, the  $(d_{x^2-y^2} + i\tau d_{xy})/\sqrt{2}$  orbital with a magnetic quantum number  $2\tau$  (refs 7,8,26). No interband optical transitions are thus allowed if only the atomic orbitals are taken into account since the change in the magnetic quantum number is  $-2\tau$  (the spin contributions are cancelled here). However, including the change in the valley orbital angular momentum (a valley pseudospin flip<sup>27</sup>), the total change in the magnetic quantum number becomes  $-\tau$ . This gives rise to the optical dipole selection rules: the direct interband transitions at the  $\text{K}$  and  $\text{K}'$  points are coupled exclusively to left and right circularly polarized light<sup>5</sup> (Fig. 1b). Detailed calculations have also shown that the selection rules hold well even for a significant portion of the  $\text{K}$  and  $\text{K}'$  valleys away from the band edges.

The photoexcited electron–hole (e–h) pairs are bound by strong Coulomb interactions in TMDs to form excitons. The influence of

the Dirac dispersion on the excitons is best viewed in terms of the hydrogen model for excitons. In this model, the electron and the hole with an effective mass derived from their band dispersions are under the influence of a central Coulomb potential  $V$ . The exciton state is labelled by  $(n, m)$ , where  $n = 0, 1, 2, \dots$  and  $m = 0, \pm 1, \pm 2, \dots$  denote the radial quantum number and the angular momentum quantum number, respectively. The states  $(n, \pm m)$  with opposite angular momentum are degenerate for conventional semiconductors with bandgap located at the  $\Gamma$  point of the Brillouin zone, a general consequence of the time-reversal symmetry. In single-layer TMDs, the bright excitons (optical dipole transition allowed) have been shown to have  $|m| = 1 \pm \tau$  for right (+) and left (−) circularly polarized light, respectively<sup>28,29</sup>. The first term ‘1’ arises from the phase winding number (=1 in single-layer TMDs), which is a topological quantity of the Bloch band and is absent in conventional semiconductors. Both the  $s$ -like ( $m = 0$ ) and  $d$ -like ( $m = 2$ ) exciton states are optically bright<sup>30</sup>. In the presence of  $N$ -fold rotational symmetry, more exciton states are bright with  $m = 1 \pm \tau + jN$ , where  $j$  is an integer<sup>28,29</sup>. On the other hand, the  $p$ -like ( $m = 1$ ) exciton states are optically dark. In this state, the electron and hole acquire an anomalous velocity in the tangential direction due to the Berry curvatures (Fig. 1e). This anomalous term breaks time-reversal symmetry in each valley and leads to an energy difference between the left-rotating ( $m = 1$ ) and right-rotating ( $m = -1$ ) states (the time-reversal symmetry is preserved including both valleys). A careful analysis shows that the energy splitting of the  $p$  levels is

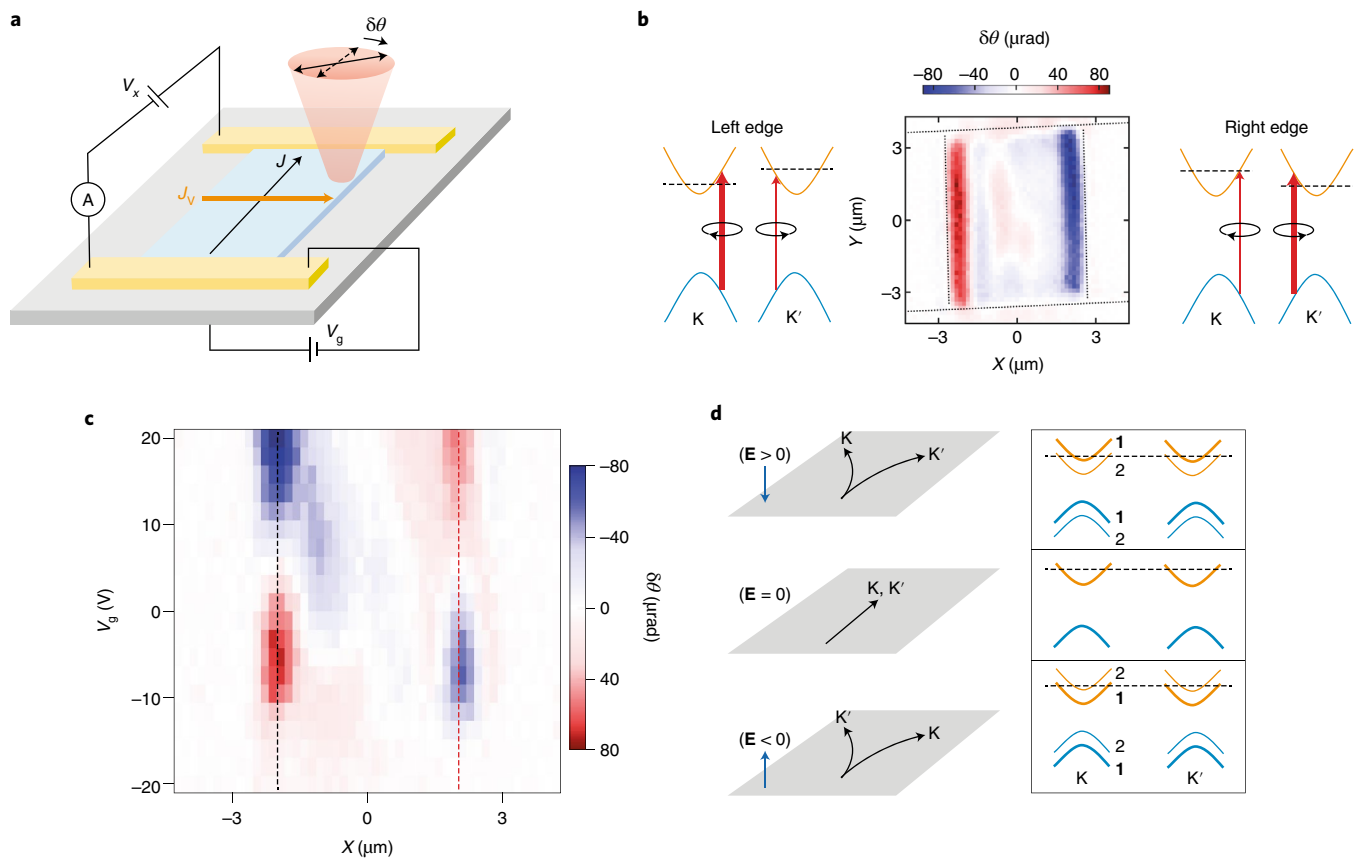


**Fig. 2 | The valley Hall effect.** **a**, Schematic of magneto-optical Kerr rotation microscopy of a back-gated transistor.  $V_g$ , gate voltage. A longitudinal electron current  $J$  drives a transverse valley current  $J_v$  by the VHE, giving rise to a Kerr rotation angle  $\delta\theta$  on sample edges. **b**, Kerr rotation image of the VHE in a  $\text{MoS}_2$  transistor by linearly polarized light near the exciton resonance. Excess K and K' electrons are accumulated on the right and left edges, respectively. **c**, Gate voltage dependence of the Kerr rotation along a horizontal cut of the channel of a bilayer  $\text{MoS}_2$  transistor (boundaries shown in vertical dotted lines).  $V_g \approx 5$  V corresponds to vertical electric field on the sample  $E = 0$ . **d**, Effect of  $E$  on the VHE in bilayer  $\text{MoS}_2$  (left) and the corresponding band dispersions (right). Bands from the top (bold) and bottom (non-bold) layers are indexed by 1 and 2, respectively, and the dashed line denotes the Fermi level of an n-doped sample. Figure adapted from: **a–c**, ref. <sup>22</sup>, Macmillan Publishers Ltd.

proportional to the Berry curvature flux penetrating the exciton envelope function in momentum space<sup>31,32</sup>.

The valley-contrasting exciton selection rules have been experimentally demonstrated for the  $1s$  ( $n = 0$ ,  $m = 0$ ) excitons in single-layer TMDs by several groups independently<sup>8,33–35</sup>. In these experiments, a large value of the photoluminescence (PL) handedness  $\rho \equiv \frac{I_+ - I_-}{I_+ + I_-}$  was observed in single-layer  $\text{MoS}_2$  upon excitation by near-resonant circularly polarized light ( $I_+$  and  $I_-$  denote, respectively, the PL intensity of the same and opposite helicity of the excitation) (Fig. 3a). Moreover, it has been shown that  $\rho$  is independent of in-plane magnetic fields up to 9 T (ref. <sup>35</sup>) (Fig. 3a). This is in contrast to optical orientation of spins in conventional semiconductors, where Hanle precession is observed<sup>36</sup>. The lack of the Hanle effect is consistent with the fact that the valley-contrasting orbital magnetic moment  $\mu_v$  is an out-of-plane vector for 2D systems and does not couple to in-plane magnetic fields. These results open the path for optical orientation of valley-polarized excitons in TMDs.

The excitonic effect in single-layer TMDs is very strong. The absorption spectrum is dominated by peaks rather than steps that are characteristic of band-to-band transitions in two dimensions<sup>12,13</sup>. An exciton binding energy in the range of 0.3–1 eV has been extracted for different TMDs from linear absorption<sup>37,38</sup>, two-photon absorption<sup>38–40</sup>, and combined scanning tunnelling microscopy and optical measurements<sup>41</sup>. The result is also consistent with the observations of charged excitons<sup>42–44</sup> and biexcitons<sup>45–47</sup> around

room temperature. It is further supported by the small exciton Bohr radius ( $\sim 1$ –2 nm) from exciton diamagnetic shift measurements up to 65 T (refs <sup>48,49</sup>). The exciton level structure in single-layer TMDs has also been examined by experiments<sup>37,38,49</sup>. From one-photon differential absorption spectra of single-layer  $\text{WS}_2$  and  $\text{WSe}_2$ , it has been possible to discern the  $1s$ ,  $2s$ ,  $3s$ ... exciton levels<sup>37,38,49</sup>. To access the one-photon ‘dark’  $p$  levels, two-photon PL excitation spectroscopy has been employed<sup>38–40</sup>. Figure 3b summarizes the exciton level structure obtained from these experiments and compares it with that of the 2D hydrogen model, 2D Dirac exciton model<sup>50</sup>, and ab initio GW-BSE (GW-Bethe–Salpeter equation) calculations<sup>51</sup> (all scaled to the same binding energy). Significant discrepancy is visible between the experimental result and the 2D hydrogen model, which predicts a much more uneven level spacing. A better agreement is obtained by the 2D Dirac exciton model discussed above<sup>50</sup>. And the best agreement is obtained by the GW-BSE calculations<sup>51</sup>, which have included effects from both the Dirac dispersion and the non-local dielectric screening of the e–h Coulomb interactions. The comparison highlights the importance of both the Dirac dispersion and the non-local dielectric screening in understanding the exciton physics in single-layer TMDs<sup>52</sup>. Finally, we note that the aforementioned finite energy splitting for the  $p$  levels from the Berry curvature effect is quite visible in both the 2D Dirac exciton model<sup>50,52</sup> and the GW-BSE calculation<sup>39,51,53–55</sup>. However, experimental results with well-resolved  $p$  levels are currently not available to verify these predictions.

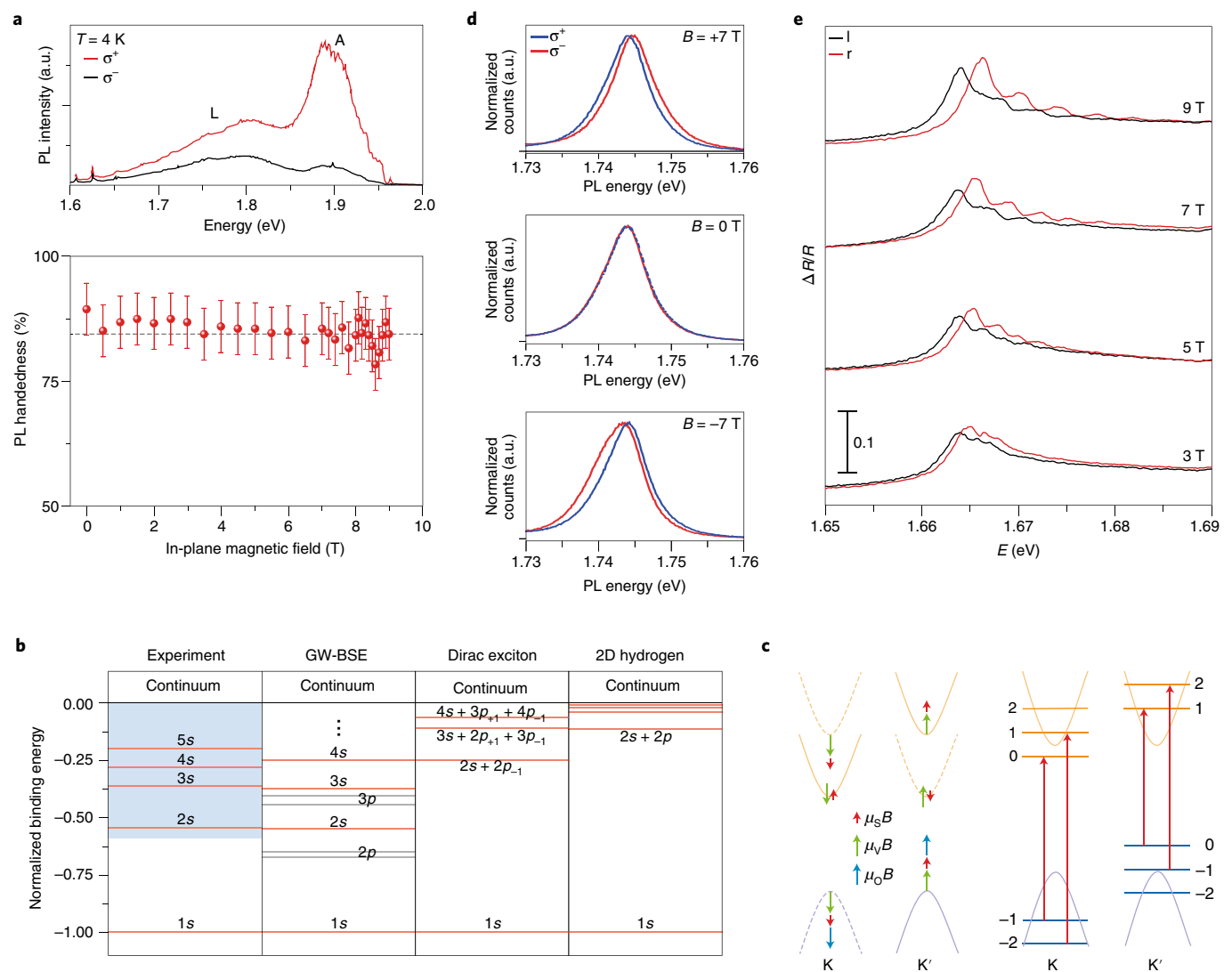


**Fig. 3 | Optical selection rules and valley magnetic response.** **a**, Experimental demonstration of valley-contrasting optical selection rules in single-layer MoS<sub>2</sub>: helicity-resolved PL under near-resonance  $\sigma^+$  pumping (top); in-plane magnetic-field dependence of the PL handedness of the A exciton (bottom). Top: L denotes the localized exciton PL. Bottom: the horizontal dashed line corresponds to the averaged PL handedness. Error bars are experimental uncertainties in the handedness. **b**, Exciton level structure of single-layer WSe<sub>2</sub> (binding energy normalized to unity) determined by different methods. Dark *p*-states (blue region) are not resolved in experiment. **c**, Left: Zeeman shift of the K and K' valleys under an out-of-plane magnetic field. The dashed and solid lines represent bands of opposite spin (split by spin-orbit coupling).  $\mu_s$ ,  $\mu_v$  and  $\mu_o$  are the spin, valley and intra-atomic orbital magnetic moments, respectively. Right: simplified LLs and inter-LL transitions (red arrows). The valley magnetic moment shifts the zero-energy LL to the band edges. **d, e**, Helicity-resolved PL (d) and reflection,  $R$ , contrast spectra (e) of single-layer WSe<sub>2</sub> under an out-of-plane magnetic field. The high sample quality in e allows the verification of the unique LL structure (right panel in c). Here  $l$  and  $r$  denote left and right circular polarizations, respectively. Figure adapted from: **a**, ref. <sup>35</sup>, APS; **b** (first and fourth columns), ref. <sup>38</sup>, APS; **b** (second column), ref. <sup>51</sup>, APS; **b** (third column), ref. <sup>50</sup>, APS; **d**, ref. <sup>58</sup>, Macmillan Publishers Ltd; **e**, ref. <sup>70</sup>, Macmillan Publishers Ltd.

**Valley magnetic response.** The valley-contrasting orbital magnetic moment  $\mu_v$  also allows the lifting of the K and K' valley degeneracy by an out-of-plane magnetic field via a Zeeman-like interaction<sup>5,7</sup>. By measuring the exciton resonance energy in the left- and right-handed polarization channels under a perpendicular magnetic field, an exciton valley Zeeman splitting of  $\sim 0.2$  meV T<sup>-1</sup> in single-layer MoSe<sub>2</sub> and WSe<sub>2</sub> has been demonstrated independently by several groups<sup>56–60</sup> (Fig. 3d). This splitting can be largely explained in the independent-particle picture by including contributions from the spin ( $\mu_s$ ), intra-atomic *d* orbital ( $\mu_o$ ) and (inter-atomic/valley) orbital ( $\mu_v$ ) magnetic moments. The orientation of these moments is sketched in Fig. 3c for the W-based compounds<sup>58</sup>. For the Mo-based compounds the spin magnetic moment for the

conduction bands reverses its direction<sup>60</sup> because the W-based and Mo-based compounds have opposite spin splitting order for the conduction bands<sup>26,61</sup>. The small valley magnetic response seems to limit the applicability of magnetic control of the valley degree of freedom in TMDs. However, recent experiments on high-quality samples with controlled doping levels have shown evidence of a significantly enhanced valley Zeeman effect driven by the strong electron–electron interactions<sup>62–65</sup>. Meanwhile, a significantly enhanced valley Zeeman effect has also been reported in coupled TMD–ferromagnetic insulator heterostructures<sup>66,67</sup>. The magnetic proximity effect induces a large exchange magnetic field on single-layer TMDs that enhances the valley magnetic response. An exchange field on the order of  $\sim 10$  T has been inferred for WSe<sub>2</sub> on EuS<sub>2</sub> (ref. <sup>66</sup>) and



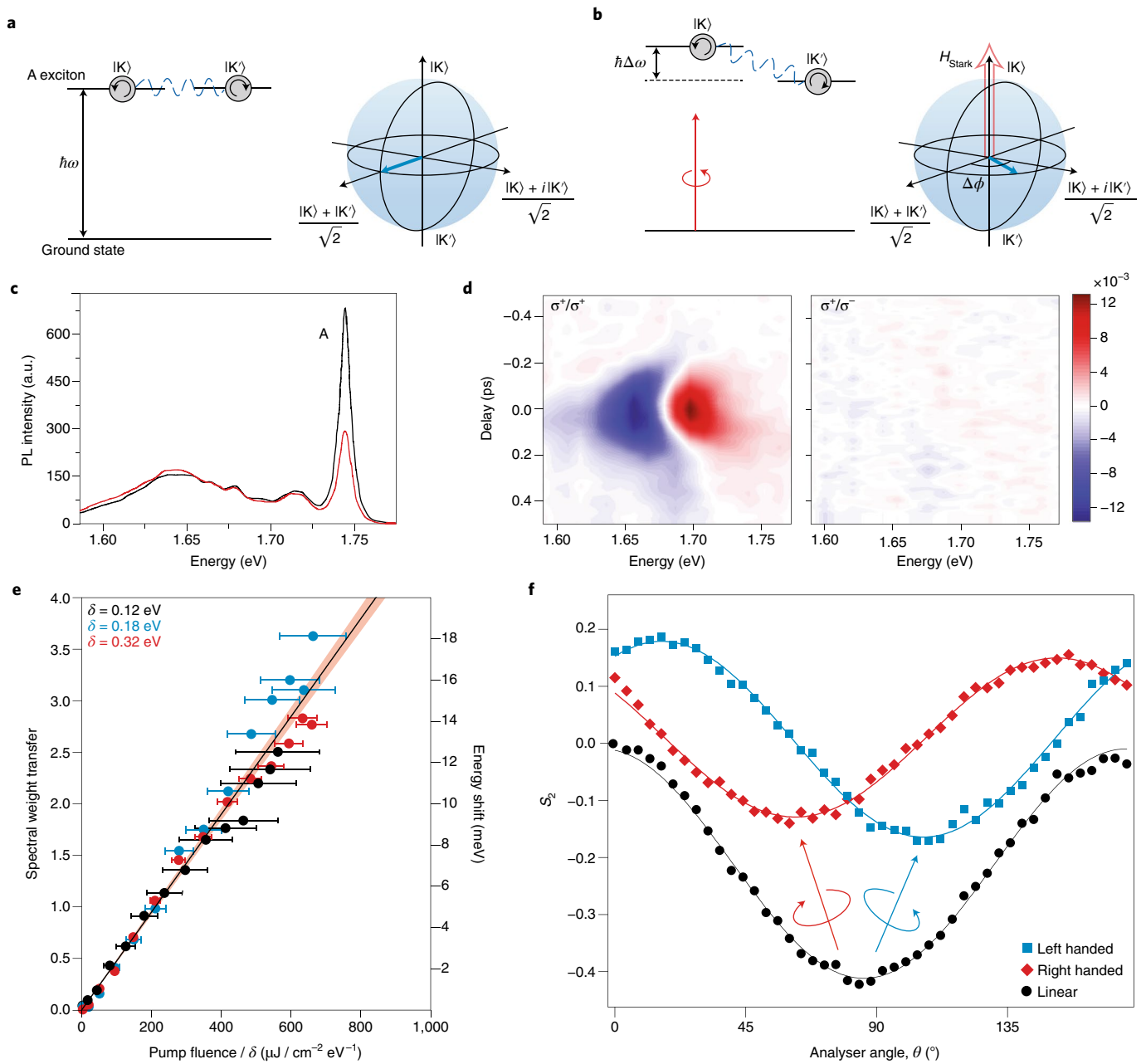


**Fig. 4 | Optical control of electronic valleys.** **a**, Linearly polarized light (blue dashed line; left) near exciton resonance creates a coherent superposition of  $|K\rangle$  and  $|K'\rangle$  exciton states, shown as the blue arrow in the Bloch sphere (right). **b**, When a strong  $\sigma^+$  below-gap control pulse (red arrow) is applied, the  $|K\rangle$  exciton energy is increased, resulting in a dynamic phase difference  $\Delta\phi$  between the two valleys. The pseudospin in the Bloch sphere is rotated by an angle  $\Delta\phi$ , just as would occur for an out-of-plane magnetic field (open arrow). **c**, Polarization-resolved PL spectra (black for s-polarization and red for p-polarization) of single-layer  $\text{WSe}_2$  under near resonance s-polarized excitation. **d**, Time- and spectral-resolved response of a  $\sigma^+$  and  $\sigma^-$  probe pulse under a  $\sigma^+$  below-gap pump pulse shows the valley-dependent optical Stark effect. **e**, Dependence of the Stark shift on pump fluence normalized by detuning  $\delta$ . The horizontal error bars correspond to the bandwidth of the pump pulse. The black line is a linear fit to the data with the orange shaded region showing the 95% confidence band. **f**, Determination of the valley pseudospin rotation by the orientation of the PL polarization. Figure adapted from: **a,b,f**, ref. <sup>85</sup>, Macmillan Publishers Ltd; **c**, ref. <sup>44</sup>, Macmillan Publishers Ltd; **d**, ref. <sup>89</sup>, AAAS; **e**, ref. <sup>90</sup>, Macmillan Publishers Ltd.

on  $\text{CrI}_3$  (ref. <sup>67</sup>), demonstrating the potential of magnetic control of the electronic valleys.

In the limit of high magnetic fields and clean samples, discrete Landau levels (LLs) form. A hallmark for the massive Dirac system is the presence of valley-polarized zero-energy LLs<sup>68,69</sup>. For a conventional 2D electron gas under an out-of-plane magnetic field  $B$ , the quantized LL energy is given by  $\varepsilon_{(v)} = (v + 1/2)\hbar\omega_c$ , where  $v = 0, 1, 2, 3, \dots$  and the cyclotron frequency  $\omega_c = \frac{eB}{m^*}$ . In TMDs, however, the valley Zeeman shift discussed above offsets  $\varepsilon_{(v)}$

by  $-\tau\hbar\omega_c/2$ , thus producing zero-energy LLs ( $\varepsilon_{(0)} = 0$ ) for the conduction band at the K valley and for the valence band at the K' valley<sup>68</sup> (Fig. 3c). The formation of discrete LLs was first observed by electrical transport measurements in single-layer TMDs fully encapsulated between hexagonal boron nitride (hBN) substrates in the relatively high doping regime<sup>14,15</sup>. Subsequently, the inter-LL transitions have been observed by performing polarization-resolved magneto-optical spectroscopy on dual-gated field-effect devices of single-layer  $\text{WSe}_2$  (ref. <sup>70</sup>) (Fig. 3e). By examining the doping

**Table 2 | Reported population lifetime, valley lifetime and valley coherence time in single-layer TMDs**

	Neutral X	Charged X	Free e <sup>-</sup>	Free h <sup>+</sup>
Population decay time	150 fs (ref. <sup>77</sup> ) (WSe <sub>2</sub> , PP) 2–5 ps (refs <sup>74–76,78</sup> ) (MoS <sub>2</sub> , MoSe <sub>2</sub> and WSe <sub>2</sub> , TPL) >10 ns (refs <sup>80,98</sup> ) (Interlayer X in MoSe <sub>2</sub> /WSe <sub>2</sub> , TPL)	10–20 ps (refs <sup>75,78</sup> ) (MoSe <sub>2</sub> and WSe <sub>2</sub> , TPL)		
Valley polarization time	<1–5 ps (refs <sup>71–73</sup> ) (MoS <sub>2</sub> and WSe <sub>2</sub> , PP, TRK and TRF) ~40 ns (ref. <sup>80</sup> ) (Interlayer X in MoSe <sub>2</sub> /WSe <sub>2</sub> , TPL)	4 ps and >> 25 ps (ref. <sup>79</sup> ) (Intervalley and intravalley trions in WSe <sub>2</sub> , PP) 1 ns (ref. <sup>75</sup> ) (WSe <sub>2</sub> , TPL)	3 ns (ref. <sup>81</sup> ) (spin, MoS <sub>2</sub> , TRK) 70 ns (ref. <sup>84</sup> ) (spin, WSe <sub>2</sub> , TRK)	80 ns (ref. <sup>82</sup> ) (WSe <sub>2</sub> , TRK) 2 μs to >40 μs (refs <sup>83,84</sup> ) (WSe <sub>2</sub> , TRK)
Valley coherence time	100–800 fs (refs <sup>85,86</sup> ) (WSe <sub>2</sub> , 2DCS and AC Stark)			

The different quasiparticles, including the neutral exciton (X), charged exciton (X), free electron (e<sup>-</sup>) and free hole (h<sup>+</sup>), are separated into columns. The different decay lifetimes are separated into rows and the experimental values are shown. The material system and the measurement technique are included in brackets. PP, pump-probe; TPL, time-resolved PL; TRK, time-resolved Kerr rotation; TRF, time-resolved Faraday rotation; 2DCS, two-dimensional coherent spectroscopy; AC Stark, time-resolved optical Stark effect.

dependence and the Shubnikov–de Haas oscillations of the optical conductivity, they have verified the presence of zero-energy LLs and determined that each LL is both valley- and spin-polarized.

### Optical control of the valley degree of freedom

The exclusive coupling of the valley excitons to photons of a particular helicity has provided a unique opportunity for the orientation and control of the valley polarization in TMDs. Two parameters, the exciton intervalley relaxation time or the valley lifetime for short ( $\tau_v$ ) and the valley exciton coherence time ( $\tau_c$ ), are of particular importance in this context. Time-resolved PL and pump-probe experiments have revealed fast exciton intervalley relaxation ( $\tau_v < 10$  ps) even at low temperatures<sup>71–73</sup>. The strong intervalley e–h exchange interaction is believed to mediate the fast depolarization<sup>72,73</sup>. At the same time, due to the strong excitonic effect and the fast non-radiative decays<sup>11</sup>, the exciton lifetime ( $\tau_x \sim$  ps) is also relatively short<sup>74–78</sup>. This explains the large steady-state PL handedness reported in the initial experiments on optical orientation of valley excitons<sup>34</sup>. Recent pump-probe experiments have reported much longer valley lifetimes for charged excitons<sup>75,79</sup> ( $\gg 25$  ps), interlayer excitons<sup>80</sup> (>10 ns) and resident carriers<sup>81–84</sup> (up to microseconds). The long valley lifetimes make these excitations promising for valley-based information storage and processing applications.

The valley exciton coherence was first demonstrated in single-layer WSe<sub>2</sub> (Fig. 4c)<sup>44</sup>. By exciting the material with linearly polarized light to prepare a coherent superposition of the K and K' valley excitons, they observed excessive PL along the excitation polarization direction (Fig. 4a). Subsequent time-resolved experiment<sup>85</sup> and 2D coherent spectroscopy<sup>86</sup> measured a decoherence time  $\tau_c \lesssim 1$  ps for valley excitons. The short valley exciton coherence time remains a challenge for applications. We summarize in Table 2 the experimental results of  $\tau_x$ ,  $\tau_v$  and  $\tau_c$  for different excitations in TMDs. We note that there are some discrepancies between the values reported for the Mo- and W-based compounds, which are not well understood. The distinct spin-polarized conduction band structures of these compounds<sup>26,61</sup> and the presence of low-lying dark exciton states in W-based compounds<sup>87,88</sup> are believed to play a role.

Another development on the optical control of the valley degree of freedom came in the form of a valley-selective optical Stark effect, that is, the optical selection rules remain valid even for non-resonant excitations. The effect has been demonstrated in single-layer WSe<sub>2</sub> (ref. <sup>89</sup>) and WS<sub>2</sub> (ref. <sup>90</sup>) by pumping with a circularly polarized femtosecond laser pulse that is red detuned from the fundamental exciton resonance. They observed a blue shift of the exciton resonance only when the probe pulse has the same handedness as the pump and when the two pulses coincide (Fig. 4d). The Stark

shift was shown to scale as  $\propto \frac{F}{\delta}$  with the (red) detuning energy  $\delta$  and the pump fluence  $F$  (Fig. 4e). A shift of ~10 meV in the valley exciton resonance has been demonstrated. Such a shift is equivalent to a Zeeman shift under a perpendicular magnetic field exceeding 50 T (refs <sup>89,90</sup>), which highlights the potential of this approach to coherently control the valley degree of freedom. We note that the above discussion is valid only for small red detuning of the optical pump from the exciton resonance. For large detuning, the off-resonance counter-rotating optical field becomes important and generates a Bloch–Siegert shift in the opposite valley (recently demonstrated in ref. <sup>91</sup>). In this case, the valley selectivity is lost.

By combining the valley-dependent optical Stark effect<sup>89,90</sup> and the optical generation of valley coherence<sup>44</sup>, coherent control of valley pseudospin in single-layer TMDs and the concept of a valley qubit for quantum computing have been demonstrated recently<sup>85</sup>. The idea is illustrated in Fig. 4a,b using a Bloch sphere to represent the SU(2) valley pseudospin space. The K and K' excitons ( $|K\rangle$  and  $|K'\rangle$ ) that point to the north and south poles, are the basis. A near-resonant linearly polarized pump pulse was used to generate a valley coherent state  $\frac{|K\rangle + |K'\rangle}{\sqrt{2}}$  in single-layer WSe<sub>2</sub>. A below-gap circularly polarized control pulse was then applied to induce an optical Stark shift  $\hbar\Delta\omega$  between the  $|K\rangle$  and  $|K'\rangle$  states. This leads to a dynamic phase difference  $\Delta\phi \sim \Delta\omega\Delta t$  between the two states for a control pulse of duration  $\Delta t$  and results in  $\frac{|K\rangle + e^{i\Delta\phi}|K'\rangle}{\sqrt{2}}$ , corresponding to a vector rotation in the equator of the Bloch sphere. The phase shift  $\Delta\phi$ , which can be varied through the control pulse intensity, was inferred from the output PL polarization (Fig. 4f). By varying the delay between the pump and control pulses, a valley exciton coherence time <1 ps has been determined<sup>85</sup>. Coherent control of the valley pseudospin in the steady state has also been demonstrated by application of a perpendicular magnetic field<sup>58,92</sup>.

### Electrical generation of valley magnetization

Practical valleytronics applications require the generation and control of the valley degree of freedom by pure electrical means<sup>93,94</sup>. The VHE discussed earlier shows the generation of valley polarization at the edges of a transistor channel of 2D TMDs by charge current. Recently, the generation of bulk valley magnetization in strained single-layer MoS<sub>2</sub> also by charge current has been reported<sup>23</sup>. The resultant valley magnetization was imaged directly by Kerr rotation microscopy (Fig. 5b). This kinematic magneto-electric effect for valleys is understood by evoking the strain effect on the valley orbital magnetic moment<sup>5</sup> (Fig. 5a). When strain breaks the three-fold rotational symmetry of the hexagonal lattice, the distribution of valley magnetic moment is shifted from the band minima<sup>23</sup>.

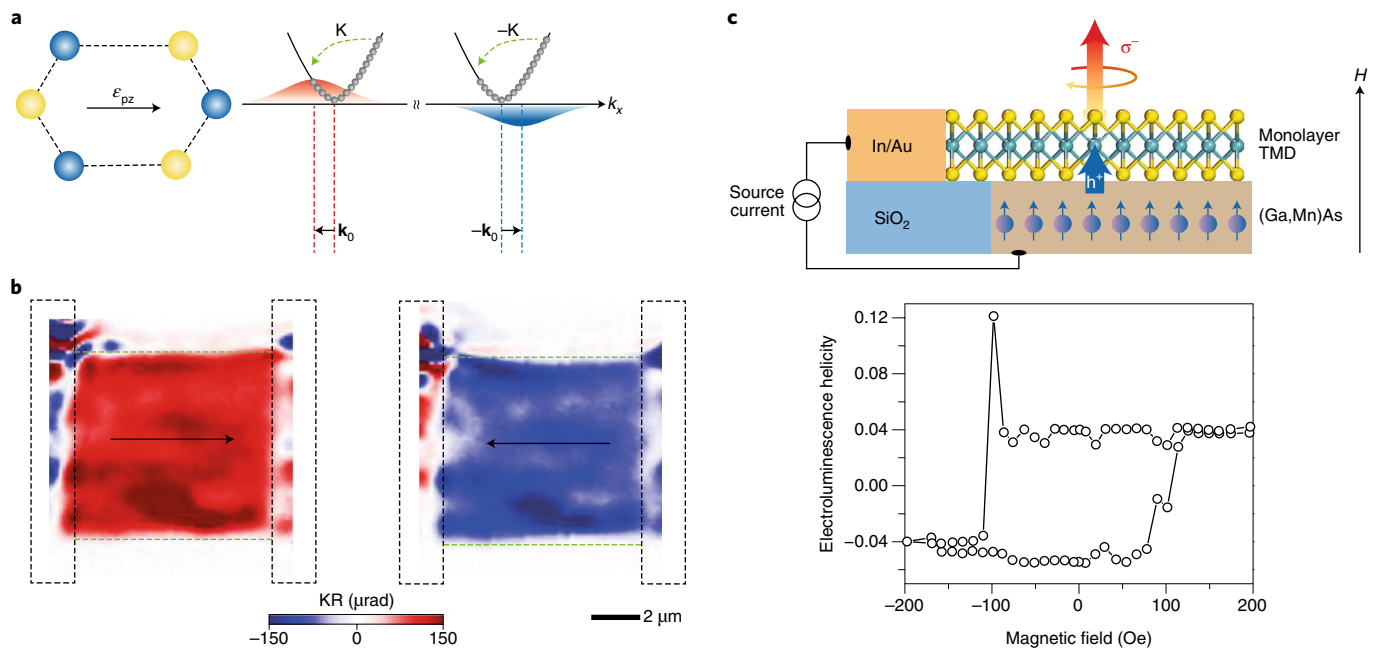


**Fig. 5 | Electrical control of electronic valleys.** **a**, Origin of the valley magnetoelectric effect in uniaxially strained single-layer MoS<sub>2</sub> (left), where  $\epsilon_{pz}$  is the local electric field along the polar axis of strained monolayer MoS<sub>2</sub>. Strain shifts the valley magnetic moment distribution (shaded peaks) away from the two valleys by  $\mathbf{k}_0$  and  $-\mathbf{k}_0$  (right). A tilted Fermi pocket due to charge current (grey spheres) encloses a different amount of orbital magnetic moment at the two valleys and generates a valley magnetization without polarization. **b**, Kerr rotation (KR) image of the resultant valley magnetization with two different current directions (black arrows). The black and green dashed lines outline the electrical contacts and the semiconductor channel, respectively. **c**, Schematic of a heterojunction consisting of a single-layer TMD and (Ga,Mn)As ferromagnetic semiconductor (top). Spins are aligned in the ferromagnetic semiconductor by an external magnetic field  $H$ . A vertical forward bias current injects spin-polarized holes into the TMD and generates circularly polarized electroluminescence. The bottom panel shows the magnetic-field dependence of the electroluminescence handedness with a clear hysteresis. Figure adapted from: **a**(left), **b**, ref. <sup>23</sup>, Macmillan Publishers Ltd; **a**(right), ref. <sup>95</sup>, Macmillan Publishers Ltd; **c**, ref. <sup>96</sup>, Macmillan Publishers Ltd.

Time-reversal symmetry requires the shift in momentum to be opposite in the two valleys. The Fermi pockets at the two valleys, however, shift along the (same) current direction and enclose different amounts of magnetic moment. A net magnetization thus emerges although no valley polarization is generated<sup>95</sup>. Electrical generation of valley polarization in single-layer TMDs has also been realized through the injection of spin-polarized carriers and spin-momentum locking in single-layer TMDs<sup>96</sup> (Fig. 5c). Using a single-layer WS<sub>2</sub>/(Ga,Mn)As heterojunction, it has been shown that spin-polarized holes can be injected from the dilute ferromagnetic semiconductor, in which spins are aligned under an external magnetic field, into single-layer WS<sub>2</sub> (ref. <sup>96</sup>). The resultant valley polarization was detected from the handedness of the electroluminescence in which the injected spin-polarized holes recombine with electrons of the same spin and same valley in WS<sub>2</sub>.

## Outlook

The field of valleytronics is progressing rapidly. Light has played a central role in the development of the basic concepts based on 2D TMDs, ranging from the orientation of valley polarization, to realization of a valley qubit, to imaging of the valley orbital magnetic moment. However, turning these concepts into viable technology presents grand challenges, at the same time, exciting opportunities. One of the challenges is to increase the valley exciton coherence time. So far, application of the valley qubits has been hindered by the short valley exciton coherence time ( $\sim$ ps) due to the rapid intravalley scattering<sup>85,86</sup>. The recent development of high-quality TMD samples through encapsulation with hBN substrates<sup>14,15,65,70</sup> has presented possibilities to prolong the valley exciton coherence time. Low-temperature electron mobility on the order of thousands of  $\text{cm}^2 \text{V}^{-1} \text{s}^{-1}$  (refs <sup>14,15</sup>) and valley polarization lifetime of tens of

microseconds<sup>83,84</sup> have already been reported in these samples. Alternatively, gate-defined quantum dots based on TMDs, the fabrication of which has been recently demonstrated<sup>97</sup>, may also significantly suppress valley exciton decoherence.

Another challenge is to develop electrical methods to inject, control and read out valley polarization or magnetization for integration with the existing technologies. While some progress has been made towards electrical injection<sup>23,93,96</sup>, electrical readout remains largely unexplored. Several valley-charge conversion schemes can be envisaged and progress in the near future is expected. The first is the inverse VHE. The effect has been demonstrated in graphene<sup>98–100</sup>, but not yet in TMDs. The second is the inverse of the magneto-electric effect discussed above that generates valley magnetization through charge current in strained single-layer MoS<sub>2</sub>. The third relies on proximity coupling of TMDs to magnetic substrates<sup>66,67</sup>. The induced valley magnetic order in TMDs can create a finite valley polarization under zero magnetic fields, which can also be read out electrically. The recent development of layered magnetic materials and the isolation of single-layer magnets<sup>101,102</sup> presents exciting opportunities for electrical injection, control and detection of valley polarization in single-layer TMDs.

Finally, we would like to mention several ongoing researches on particles or quasiparticles other than electrons that also possess the valley degree of freedom. For instance, exciton-polaritons with valleys addressable by photons have been realized in coupled TMD-optical cavities<sup>103</sup>. These hybrid systems may be used to realize valley lasers, for which gain and lasing occur only in one valley. In addition, valley plasmons that can support chiral edge modes have been predicted in gapped Dirac systems with broken time reversal symmetry<sup>104,105</sup>. Meanwhile, topological edge states arising from the VHE for light have been demonstrated in 2D honeycomb photonic



lattices with broken inversion symmetry<sup>106,107</sup>. These different research directions are intertwined and stimulated by one another. The outlook of valleytronics is exciting.

Received: 5 February 2018; Accepted: 1 June 2018;  
Published online: 27 July 2018

## References

1. Takashina, K., Ono, Y., Fujiwara, A., Takahashi, Y. & Hirayama, Y. Valley polarization in Si(100) at zero magnetic field. *Phys. Rev. Lett.* **96**, 236801 (2006).
2. Isberg, J. et al. Generation, transport and detection of valley-polarized electrons in diamond. *Nat. Mater.* **12**, 760–764 (2013).
3. Gunawan, O. et al. Valley susceptibility of an interacting two-dimensional electron system. *Phys. Rev. Lett.* **97**, 186404 (2006).
4. Zhu, Z., Collaudin, A., Fauque, B., Kang, W. & Behnia, K. Field-induced polarization of Dirac valleys in bismuth. *Nat. Phys.* **8**, 89–94 (2012).
5. Xiao, D., Yao, W. & Niu, Q. Valley-contrasting physics in graphene: magnetic moment and topological transport. *Phys. Rev. Lett.* **99**, 236809 (2007).
6. Yao, W., Xiao, D. & Niu, Q. Valley-dependent optoelectronics from inversion symmetry breaking. *Phys. Rev. B* **77**, 235406 (2008).
7. Xiao, D., Liu, G.-B., Feng, W., Xu, X. & Yao, W. Coupled spin and valley physics in monolayers of MoS<sub>2</sub> and other group-VI dichalcogenides. *Phys. Rev. Lett.* **108**, 196802 (2012).
8. Cao, T. et al. Valley-selective circular dichroism of monolayer molybdenum disulphide. *Nat. Commun.* **3**, 887 (2012).
9. Jia, S., Xu, S.-Y. & Hasan, M. Z. Weyl semimetals, Fermi arcs and chiral anomalies. *Nat. Mater.* **15**, 1140–1144 (2016).
10. Ma, Q. et al. Direct optical detection of Weyl fermion chirality in a topological semimetal. *Nat. Phys.* **13**, 842–847 (2017).
11. Mak, K. F. & Shan, J. Photonics and optoelectronics of 2D semiconductor transition metal dichalcogenides. *Nat. Photon.* **10**, 216–226 (2016).
12. Splendiani, A. et al. Emerging photoluminescence in monolayer MoS<sub>2</sub>. *Nano Lett.* **10**, 1271–1275 (2010).
13. Mak, K. F., Lee, C., Hone, J., Shan, J. & Heinz, T. F. Atomically thin MoS<sub>2</sub>: a new direct-gap semiconductor. *Phys. Rev. Lett.* **105**, 136805 (2010).
14. Cui, X. et al. Multi-terminal transport measurements of MoS<sub>2</sub> using a van der Waals heterostructure device platform. *Nat. Nanotech.* **10**, 534–540 (2015).
15. Fallahazad, B. et al. Shubnikov-de Haas oscillations of high-mobility holes in monolayer and bilayer WSe<sub>2</sub>: Landau level degeneracy, effective mass, and negative compressibility. *Phys. Rev. Lett.* **116**, 086601 (2016).
16. Xu, X., Yao, W., Xiao, D. & Heinz, T. F. Spin and pseudospins in layered transition metal dichalcogenides. *Nat. Phys.* **10**, 343–350 (2014).
17. Manzeli, S., Ovchinnikov, D., Pasquier, D., Yazyev, O. V. & Kis, A. 2D transition metal dichalcogenides. *Nat. Rev. Mater.* **2**, 17033 (2017).
18. Schaibley, J. R. et al. Valleytronics in 2D materials. *Nat. Rev. Mater.* **1**, 16055 (2016).
19. Xiao, D., Chang, M.-C. & Niu, Q. Berry phase effects on electronic properties. *Rev. Mod. Phys.* **82**, 1959–2007 (2010).
20. Lensky, Y. D., Song, J. C. W., Samutpraphoot, P. & Levitov, L. S. Topological valley currents in gapped Dirac materials. *Phys. Rev. Lett.* **114**, 256601 (2015).
21. Mak, K. F., McGill, K. L., Park, J. & McEuen, P. L. The valley Hall effect in MoS<sub>2</sub> transistors. *Science* **344**, 1489–1492 (2014).
22. Lee, J., Mak, K. F. & Shan, J. Electrical control of the valley Hall effect in bilayer MoS<sub>2</sub> transistors. *Nat. Nanotech.* **11**, 421–425 (2016).
23. Lee, J., Wang, Z., Xie, H., Mak, K. F. & Shan, J. Valley magnetoelectricity in single-layer MoS<sub>2</sub>. *Nat. Mater.* **16**, 887–891 (2017).
24. Kato, Y. K., Myers, R. C., Gossard, A. C. & Awschalom, D. D. Observation of the spin Hall effect in semiconductors. *Science* **306**, 1910–1913 (2004).
25. Wu, S. et al. Electrical tuning of valley magnetic moment through symmetry control in bilayer MoS<sub>2</sub>. *Nat. Phys.* **9**, 149–153 (2013).
26. Liu, G.-B., Shan, W.-Y., Yao, Y., Yao, W. & Xiao, D. Three-band tight-binding model for monolayers of group-VIB transition metal dichalcogenides. *Phys. Rev. B* **88**, 085433 (2013).
27. Mecklenburg, M. & Regan, B. C. Spin and the honeycomb lattice: lessons from graphene. *Phys. Rev. Lett.* **106**, 116803 (2011).
28. Cao, T., Wu, M. & Louie, S. G. Unifying optical selection rules for excitons in two dimensions: band topology and winding numbers. *Phys. Rev. Lett.* **120**, 087402 (2018).
29. Zhang, X., Shan, W.-Y. & Xiao, D. Optical selection rule of excitons in gapped chiral fermion systems. *Phys. Rev. Lett.* **120**, 077401 (2018).
30. Gong, P., Yu, H., Wang, Y. & Yao, W. Optical selection rules for excitonic Rydberg series in the massive Dirac cones of hexagonal two-dimensional materials. *Phys. Rev. B* **95**, 125420 (2017).
31. Srivastava, A. & Imamoğlu, A. Signatures of Bloch-band geometry on excitons: nonhydrogenic spectra in transition-metal dichalcogenides. *Phys. Rev. Lett.* **115**, 166802 (2015).
32. Zhou, J., Shan, W.-Y., Yao, W. & Xiao, D. Berry phase modification to the energy spectrum of excitons. *Phys. Rev. Lett.* **115**, 166803 (2015).
33. Zeng, H., Dai, J., Yao, W., Xiao, D. & Cui, X. Valley polarization in MoS<sub>2</sub> monolayers by optical pumping. *Nat. Nanotech.* **7**, 490–493 (2012).
34. Mak, K. F., He, K., Shan, J. & Heinz, T. F. Control of valley polarization in monolayer MoS<sub>2</sub> by optical helicity. *Nat. Nanotech.* **7**, 494–498 (2012).
35. Sallen, G. et al. Robust optical emission polarization in MoS<sub>2</sub> monolayers through selective valley excitation. *Phys. Rev. B* **86**, 081301 (2012).
36. Žutić, I., Fabian, J. & Das Sarma, S. Spintronics: fundamentals and applications. *Rev. Mod. Phys.* **76**, 323–410 (2004).
37. Chernikov, A. et al. Exciton binding energy and nonhydrogenic Rydberg series in monolayer WS<sub>2</sub>. *Phys. Rev. Lett.* **113**, 076802 (2014).
38. He, K. et al. Tightly bound excitons in monolayer WSe<sub>2</sub>. *Phys. Rev. Lett.* **113**, 026803 (2014).
39. Ye, Z. et al. Probing excitonic dark states in single-layer tungsten disulphide. *Nature* **513**, 214–218 (2014).
40. Wang, G. et al. Giant enhancement of the optical second-harmonic emission of WSe<sub>2</sub> monolayers by laser excitation at exciton resonances. *Phys. Rev. Lett.* **114**, 097403 (2015).
41. Ugeda, M. M. et al. Giant bandgap renormalization and excitonic effects in a monolayer transition metal dichalcogenide semiconductor. *Nat. Mater.* **13**, 1091–1095 (2014).
42. Mak, K. F. et al. Tightly bound trions in monolayer MoS<sub>2</sub>. *Nat. Mater.* **12**, 207–211 (2013).
43. Ross, J. S. et al. Electrical control of neutral and charged excitons in a monolayer semiconductor. *Nat. Commun.* **4**, 1474 (2013).
44. Jones, A. M. et al. Optical generation of excitonic valley coherence in monolayer WSe<sub>2</sub>. *Nat. Nanotech.* **8**, 634–638 (2013).
45. You, Y. et al. Observation of biexcitons in monolayer WSe<sub>2</sub>. *Nat. Phys.* **11**, 477–481 (2015).
46. Sie, E. J., Frenzel, A. J., Lee, Y.-H., Kong, J. & Gedik, N. Intervalley biexcitons and many-body effects in monolayer MoS<sub>2</sub>. *Phys. Rev. B* **92**, 125417 (2015).
47. Shang, J. et al. Observation of excitonic fine structure in a 2D transition-metal dichalcogenide semiconductor. *ACS Nano* **9**, 647–655 (2015).
48. Stier, A. V., McCreary, K. M., Jonker, B. T., Kono, J. & Crooker, S. A. Exciton diamagnetic shifts and valley Zeeman effects in monolayer WS<sub>2</sub> and MoS<sub>2</sub> to 65 Tesla. *Nat. Commun.* **7**, 10643 (2016).
49. Stier, A. V. et al. Magnetooptics of exciton Rydberg states in a monolayer semiconductor. *Phys. Rev. Lett.* **120**, 057405 (2017).
50. Trushin, M., Goerbig, M. O. & Belzig, W. Optical absorption by Dirac excitons in single-layer transition-metal dichalcogenides. *Phys. Rev. B* **94**, 041301 (2016).
51. Qiu, D. Y., da Jornada, F. H. & Louie, S. G. Optical spectrum of MoS<sub>2</sub>: many-body effects and diversity of exciton states. *Phys. Rev. Lett.* **111**, 216805 (2013).
52. Trushin, M., Goerbig, M. O. & Belzig, W. Model prediction of self-rotating excitons in two-dimensional transition-metal dichalcogenides. Preprint at <https://arxiv.org/abs/1708.03638> (2017).
53. Ramasubramanian, A. Large excitonic effects in monolayers of molybdenum and tungsten dichalcogenides. *Phys. Rev. B* **86**, 115409 (2012).
54. Wu, F., Qu, F. & MacDonald, A. H. Exciton band structure of monolayer MoS<sub>2</sub>. *Phys. Rev. B* **91**, 075310 (2015).
55. Berkelbach, T. C., Hybertsen, M. S. & Reichman, D. R. Bright and dark singlet excitons via linear and two-photon spectroscopy in monolayer transition-metal dichalcogenides. *Phys. Rev. B* **92**, 085413 (2015).
56. MacNeill, D. et al. Breaking of valley degeneracy by magnetic field in monolayer MoSe<sub>2</sub>. *Phys. Rev. Lett.* **114**, 037401 (2015).
57. Li, Y. et al. Valley splitting and polarization by the Zeeman effect in Monolayer MoSe<sub>2</sub>. *Phys. Rev. Lett.* **113**, 266804 (2014).
58. Aivazian, G. et al. Magnetic control of valley pseudospin in monolayer WSe<sub>2</sub>. *Nat. Phys.* **11**, 148–152 (2015).
59. Srivastava, A. et al. Valley Zeeman effect in elementary optical excitations of monolayer WSe<sub>2</sub>. *Nat. Phys.* **11**, 141–147 (2015).
60. Wang, G. et al. Magneto-optics in transition metal diselenide monolayers. *2D Mater.* **2**, 034002 (2015).
61. Wang, Z., Zhao, L., Mak, K. F. & Shan, J. Probing the spin-polarized electronic band structure in monolayer transition metal dichalcogenides by optical spectroscopy. *Nano Lett.* **17**, 740–746 (2017).
62. Movva, H. C. P. et al. Density-dependent quantum Hall states and Zeeman splitting in monolayer and bilayer WSe<sub>2</sub>. *Phys. Rev. Lett.* **118**, 247701 (2017).
63. Back, P. et al. Giant paramagnetism-induced valley polarization of electrons in charge-tunable monolayer MoSe<sub>2</sub>. *Phys. Rev. Lett.* **118**, 237404 (2017).
64. Wang, Z., Mak, K. F. & Shan, J. Strongly interaction-enhanced valley magnetic response in monolayer WSe<sub>2</sub>. *Phys. Rev. Lett.* **120**, 066402 (2017).
65. Gustafsson, M. V. et al. Ambipolar Landau levels and strong band-selective carrier interactions in monolayer WSe<sub>2</sub>. *Nat. Mater.* **17**, 411–415 (2018).
66. Zhao, C. et al. Enhanced valley splitting in monolayer WSe<sub>2</sub> due to magnetic exchange field. *Nat. Nanotech.* **12**, 757–762 (2017).

67. Zhong, D. et al. Van der Waals engineering of ferromagnetic semiconductor heterostructures for spin and valleytronics. *Sci. Adv.* **3**, e1603113 (2017).
68. Cai, T. et al. Magnetic control of the valley degree of freedom of massive Dirac fermions with application to transition metal dichalcogenides. *Phys. Rev. B* **88**, 115140 (2013).
69. Li, X., Zhang, F. & Niu, Q. Unconventional quantum Hall effect and tunable spin Hall effect in Dirac materials: application to an isolated  $\text{MoS}_2$  trilayer. *Phys. Rev. Lett.* **110**, 066803 (2013).
70. Wang, Z., Shan, J. & Mak, K. F. Valley- and spin-polarized Landau levels in monolayer  $\text{WSe}_2$ . *Nat. Nanotech.* **12**, 144–149 (2017).
71. Zhu, C. R. et al. Exciton valley dynamics probed by Kerr rotation in  $\text{WSe}_2$  monolayers. *Phys. Rev. B* **90**, 161302 (2014).
72. Mai, C. et al. Many-body effects in valleytronics: direct measurement of valley lifetimes in single-layer  $\text{MoS}_2$ . *Nano Lett.* **14**, 202–206 (2014).
73. Dal Conte, S. et al. Ultrafast valley relaxation dynamics in monolayer  $\text{MoS}_2$  probed by nonequilibrium optical techniques. *Phys. Rev. B* **92**, 235425 (2015).
74. Korn, T., Heydrich, S., Hirmer, M., Schmutzler, J. & Schüller, C. Low-temperature photocarrier dynamics in monolayer  $\text{MoS}_2$ . *Appl. Phys. Lett.* **99**, 102109 (2011).
75. Wang, G. et al. Valley dynamics probed through charged and neutral exciton emission in monolayer  $\text{WSe}_2$ . *Phys. Rev. B* **90**, 075413 (2014).
76. Lagarde, D. et al. Carrier and polarization dynamics in monolayer  $\text{MoS}_2$ . *Phys. Rev. Lett.* **112**, 047401 (2014).
77. Poellmann, C. et al. Resonant internal quantum transitions and femtosecond radiative decay of excitons in monolayer  $\text{WSe}_2$ . *Nat. Mater.* **14**, 889–893 (2015).
78. Robert, C. et al. Exciton radiative lifetime in transition metal dichalcogenide monolayers. *Phys. Rev. B* **93**, 205423 (2016).
79. Singh, A. et al. Long-lived valley polarization of intravalley trions in monolayer  $\text{WSe}_2$ . *Phys. Rev. Lett.* **117**, 257402 (2016).
80. Rivera, P. et al. Valley-polarized exciton dynamics in a 2D semiconductor heterostructure. *Science* **351**, 688–691 (2016).
81. Yang, L. et al. Long-lived nanosecond spin relaxation and spin coherence of electrons in monolayer  $\text{MoS}_2$  and  $\text{WS}_2$ . *Nat. Phys.* **11**, 830–834 (2015).
82. Song, X., Xie, S., Kang, K., Park, J. & Sih, V. Long-lived hole spin/valley polarization probed by Kerr rotation in monolayer  $\text{WSe}_2$ . *Nano Lett.* **16**, 5010–5014 (2016).
83. Kim, J. et al. Observation of ultralong valley lifetime in  $\text{WSe}_2/\text{MoS}_2$  heterostructures. *Sci. Adv.* **3**, e1700518 (2017).
84. Dey, P. et al. Gate-controlled spin-valley locking of resident carriers in  $\text{WSe}_2$  monolayers. *Phys. Rev. Lett.* **119**, 137401 (2017).
85. Ye, Z., Sun, D. & Heinz, T. F. Optical manipulation of valley pseudospin. *Nat. Phys.* **13**, 26–29 (2017).
86. Hao, K. et al. Direct measurement of exciton valley coherence in monolayer  $\text{WSe}_2$ . *Nat. Phys.* **12**, 677–682 (2016).
87. Zhang, X.-X. et al. Magnetic brightening and control of dark excitons in monolayer  $\text{WSe}_2$ . *Nat. Nanotech.* **12**, 883–888 (2017).
88. Zhou, Y. et al. Probing dark excitons in atomically thin semiconductors via near-field coupling to surface plasmon polaritons. *Nat. Nanotech.* **12**, 856–860 (2017).
89. Kim, J. et al. Ultrafast generation of pseudo-magnetic field for valley excitons in  $\text{WSe}_2$  monolayers. *Science* **346**, 1205–1208 (2014).
90. Sie, E. J. et al. Valley-selective optical Stark effect in monolayer  $\text{WS}_2$ . *Nat. Mater.* **14**, 290–294 (2015).
91. Sie, E. J. et al. Large, valley-exclusive Bloch-Siegert shift in monolayer  $\text{WS}_2$ . *Science* **355**, 1066–1069 (2017).
92. Wang, G. et al. Control of exciton valley coherence in transition metal dichalcogenide monolayers. *Phys. Rev. Lett.* **117**, 187401 (2016).
93. Zhang, Y. J., Oka, T., Suzuki, R., Ye, J. T. & Iwasa, Y. Electrically switchable chiral light-emitting transistor. *Science* **344**, 725–728 (2014).
94. An, X.-T. et al. Realization of valley and spin pumps by scattering at nonmagnetic disorders. *Phys. Rev. Lett.* **118**, 096602 (2017).
95. Yu, H. & Yao, W. Valleytronics: magnetization without polarization. *Nat. Mater.* **16**, 876–877 (2017).
96. Ye, Y. et al. Electrical generation and control of the valley carriers in a monolayer transition metal dichalcogenide. *Nat. Nanotech.* **11**, 598–602 (2016).
97. Wang, K. et al. Electrical control of charged carriers and excitons in atomically thin materials. *Nat. Nanotech.* **13**, 128–132 (2018).
98. Gorbachev, R. V. et al. Detecting topological currents in graphene superlattices. *Science* **346**, 448–451 (2014).
99. Shimazaki, Y. et al. Generation and detection of pure valley current by electrically induced Berry curvature in bilayer graphene. *Nat. Phys.* **11**, 1032–1036 (2015).
100. Sui, M. et al. Gate-tunable topological valley transport in bilayer graphene. *Nat. Phys.* **11**, 1027–1031 (2015).
101. Gong, C. et al. Discovery of intrinsic ferromagnetism in two-dimensional van der Waals crystals. *Nature* **546**, 265–269 (2017).
102. Huang, B. et al. Layer-dependent ferromagnetism in a van der Waals crystal down to the monolayer limit. *Nature* **546**, 270–273 (2017).
103. Chen, Y.-J., Cain, J. D., Stanev, T. K., Dravid, V. P. & Stern, N. P. Valley-polarized exciton-polaritons in a monolayer semiconductor. *Nat. Photon.* **11**, 431–435 (2017).
104. Song, J. C. W. & Rudner, M. S. Chiral plasmons without magnetic field. *Proc. Natl Acad. Sci. USA* **113**, 4658–4663 (2016).
105. Kumar, A. et al. Chiral plasmon in gapped Dirac systems. *Phys. Rev. B* **93**, 041413 (2016).
106. Noh, J., Huang, S., Chen, K. & Rechtsman, M. C. Observation of photonic topological valley Hall edge states. *Phys. Rev. Lett.* **120**, 063902 (2017).
107. Tzuhuan, M. & Gennady, S. All-Si valley-Hall photonic topological insulator. *New J. Phys.* **18**, 025012 (2016).
108. Wang, Z., Chiu, Y.-H., Honz, K., Mak, K. F. & Shan, J. Electrical tuning of interlayer exciton gases in  $\text{WSe}_2$  bilayers. *Nano Lett.* **18**, 137–143 (2018).

## Acknowledgements

We acknowledge support from US Department of Energy (DOE) BES grant no. DESC0013883, Air Force Office of Scientific Research under grant FA9550-16-1-0249 and a David and Lucille Packard Fellowship and a Sloan Fellowship (K.F.M.); from DOE BES grant no. DE-SC0012509, National Science Foundation (NSF) grant no. EFRI-1433496, and a Cottrell Scholar Award (D.X.); and from NSF grant no. 1410407 and 1420451 (J.S.).

## Competing interests

The authors declare no competing interests.

## Additional information

Reprints and permissions information is available at [www.nature.com/reprints](http://www.nature.com/reprints).

Correspondence should be addressed to K.F.M. or D.X. or J.S.

**Publisher's note:** Springer Nature remains neutral with regard to jurisdictional claims in published maps and institutional affiliations.